

Imaging vasodynamics in the awake mouse brain with two-photon microscopy

Andy Y. Shih¹, Patrick J. Drew^{2,3} and David Kleinfeld^{4,5}

¹Department of Neurosciences, Medical University of South Carolina, SC, USA

²Department of Engineering Science & Mechanics, Pennsylvania State University, University Park, PA, USA

³Department of Neurosurgery, Pennsylvania State University, University Park, PA, USA

⁴Department of Physics, University of California at San Diego, La Jolla, CA, USA

⁵Section of Neurobiology, University of California at San Diego, La Jolla, CA, USA

To appear in "Neurovascular Coupling Methods", Theodore H. Schwartz, editor, as part of the NEUROMETHODS series, Wolfgang Walz, series editor, by Springer Science + Business Media

Text	4450 words
Displayed Items	5 figures (all in color)
References	52

Abbreviations:

ACSF = artificial cerebral spinal fluid

BOLD fMRI = blood oxygen level dependent functional magnetic resonance imaging

PoRTS = polished and reinforced thinned skull

RBC = red blood cell

TPLSM = two-photon laser scanning microscopy

Keywords: Arterioles, blood flow, capillary, cortex, cranial window, mouse, rat, stroke, transcranial window, venules.

Editorial correspondence:

David Kleinfeld
Department of Physics
University of California 0374
9500 Gilman Drive
La Jolla, CA 92093-0374
E-mail: dk@physics.ucsd.edu.

Abstract

In vivo two-photon laser-scanning microscopy is widely used to study brain structure and function in mice. Recent studies using awake mice have revealed a rich dynamism in cerebrovascular flow and neural activity that is significantly masked by anesthesia. Imaging of awake animals is necessary to fully understand neurovascular coupling during naturalistic sensorimotor activity. We provide detailed instructions to rigorously quantify blood flow at the level of single cortical vessels in awake mice. This includes a description of surgical techniques to obtain optical access to the cortex, improved head-restraint devices to reduce motion artifacts, and robust algorithms to quantify red blood cell flow and vessel caliber. Finally, we provide examples on how these techniques are used to measure sensory-evoked cortical hemodynamics.

1. Background

The moment-to-moment energy demands of neuronal computation in the mammalian brain are high, yet the brain has limited reserves of energy [1, 2]. A solution to this dilemma calls for a vascular system that functions as a reliable, pervasive supply chain. With regard to the cortical mantle, this system begins with the great cerebral arteries that emanate from the Circle of Willis and source a planar network of highly interconnected pial arterioles that span the surface of the mantle [3]. The inherent multitude of paths for flow to any given branch allows the surface network to distribute blood in a manner that is relatively insensitive to blockages in one or a few branches of the network [4, 5]. Further, the distribution can be dynamically shifted toward regions of heightened electrical activity and concurrent metabolic load [6, 7]. The surface network is connected to an underlying, three-dimensional network of microvessels by radially directed penetrating arterioles (**Fig. 4-1**). The microvascular network forms a completely interconnected network such that flow may occur in any direction [8]. This network is drained by penetrating venules that return blood to the surface of cortex, where it empties into the central sinus to complete the supply chain (**Fig. 4-1**). While the microvascular network brokers the bulk of the exchange of metabolites and gases between brain cells and the blood stream, the mechanism for the control of flow in these vessels remains an open issue.

Figure 4-1 goes about here.

In vivo two-photon laser-scanning microscopy (TPLSM) is an established method to visualize cerebrovascular topology and quantify blood flow at the level of single vessels in the rodent cortex [9, 10]. In this respect, TPLSM has become a key tool to understand the basis of neurovascular coupling [11]. While a rich body of data has resulted from studies on anesthetized animals, there remains a striking paucity of studies on vasodynamics in the awake state. Anesthetics greatly dampen the activity of neurons [12] and astrocytes [13], and alter vascular dynamics in basal and stimulated states [14]. Anesthetics further preclude the study of vascular function during voluntary sensorimotor function. To image brain vasculature in the awake state, only minor enhancements upon routine *in vivo* imaging techniques are necessary. First, chronically implanted cranial windows are required to allow imaging well after recovery from initial surgeries. Second, a rigid head mount and gradual habituation to head restraint is needed to minimize movement during imaging. In this chapter, we describe methods to visualize and quantify blood flow at the level of individual vessels in the cerebral cortex of awake, head-restrained mice. We further provide an example of how this technique can be used to study the effects of sensory-evoked neuronal activity on vascular responses.

1.1 Visualizing the cerebral vasculature.

A portion of the overlying skull must be thinned to translucency or removed entirely to gain optical access to the mouse cortex. Detailed methods have been described for chronic bone-removed cranial windows [15, 16] and semi-chronic thinned skull windows [17] and will not be discussed further. Thinned skull windows are preferred for experiments since exposure of the cortex to air, compression of the brain with an overlying coverslip, and mechanical disturbances can cause inflammation and gliosis that might affect the phenomenon under study [18]. However, thinned skull windows are limited in imaging depth, allowing optical access to the upper 250 μm of cortex with conventional TPLSM imaging systems. To study deeper cortical layers, one must use bone-removed cranial window, which can provide access to cortical structures as deep as 600 to 800 μm , or even the full 1 mm depth of cortex with special techniques [19]. Thus, the type of window used depends largely upon the goal of the experiment, and the factors to consider are imaging depth and potential affects of surgically-induced inflammation.

Without structural support, the thinned skull is flexible and movement artifacts caused by heart-beat or breathing will affect imaging of small structures. Past studies have avoided

this issue by generating very small windows in order to maintain rigidity, *i.e.*, less than 200 μm in diameter [17]. However, larger windows are needed to study vasodynamics since the position of arterioles and venules cannot be readily predicted before window construction. We thus highlight a method to generate a relatively large, chronic thinned-skull cranial window in mice, *i.e.*, a 2 mm in diameter PoRTS window, where the skull is reinforced with a thin layer of glue and cover glass for rigidity and to impede bone regrowth (**Fig. 4-2**) [20, 21]. The result is a cranial window that can be used image pial arterioles, venules, and microvessels in the upper cortical layers (**Fig. 4-2m**) for over one month (**Fig. 4-2n**) [20].

Figure 4-2 goes about here.

2. Materials for PoRTS window preparation

2.1 Reagents.

- Isoflurane (029405; Butler Schein).
- Betadine (6906950; Butler Schein).
- Buprenorphine hydrochloride (Buprenex®) (031919; Butler Schein).
- Fluorescein-dextran (FD2000S; Sigma) or Texas Red-dextran (D1830; Invitrogen).
- Isopropyl alcohol, diluted to 70 % (v/v) in water (I9030; Sigma-Aldrich).
- Lactated Ringer's solution (009846; Butler Schein).
- Artificial cerebral spinal fluid (ACSF). Prepared from 125 mM NaCl, 5 mM KCl , 10 mM glucose, 10 mM HEPES, 3.1 mM CaCl_2 , 1.3 mM MgCl_2 , pH 7.4. Sterile filter and maintain as aliquots at 4°C.

2.2 Disposables.

- Cotton-tipped applicators (23-400-100; Fisher Scientific).
- Cover Glass, no. 0 thickness (6661B40; Thomas Scientific).
- Cyanoacrylate glue (31428 H04308; ND Industries).
- Bone wax (032005; Butler Schein).
- Dental cement (S380; Metabond, Parkell).

- Drill burrs (19007-05; Fine Science Tools).
- Insulin syringe, 0.3 mL volume with 29.5 gauge needle (309301; Fisher).
- Kimwipes (06-666A; Fisher Scientific).
- Ophthalmic ointment (039886; Butler Schein).
- Scalpel blades (12-460-448; Fisher Scientific).
- Silicone aquarium sealant (31001; Perfecto Manufacturing).
- Tin oxide powder (EQT-TINOX; Mama's Minerals).

2.3 Equipment.

- Electric powered dental drill (EXL-M40; Osada).
- Stereo Microscope (SVX16; Olympus, or similar system).
- Electrical razor (Series 8900; Wahl).
- Forceps, Dumont no. 55 (11255-20; Fine Science Tools).
- Forceps, serrated (11050-10; Fine Science Tools).
- Glass scribe to cut cover glass (08-675; Fisher Scientific).
- Heating pad with feedback regulation (Temperature control system, 40-90-8, rectal thermistor, 40-90-5D-02, and heat pad for mouse, 40-90-2-07; FHC Inc.).
- Isoflurane vaporizer (IsoTec4; Datex-Ohmeda, GE Healthcare).
- Stereotaxic frame (Model 900 stereotaxic frame, Model 923-B mouse gas anesthesia head holder, Model 922 non-rupture 60° tip ear bars; David Kopf).
- Surgical scissors, blunt end (14078-10; Fine Science Tools).
- Custom-made head-frame [20].

3. Procedure

3.1 Surgery for PoRTS window preparation

1. Induce anesthesia. Ensure a surgical plane of anesthesia by checking for lack of toe

pinch reflex.

2. Secure animal in stereotaxic frame [22].
3. Maintain body temperature with feed-back regulated heat pad.
4. Apply ophthalmic ointment to eyes to retain moisture.
5. Shave the scalp with an electrical razor.
6. Clean the scalp with Betadine followed by 70 % (v/v) isopropyl alcohol.
7. Using sterilized tools, remove the scalp over the entire dorsal skull surface (**Fig. 4-2a**). Use a scalpel blade to remove the thin periosteum from the surface of the skull.
8. Clean and dry the skull surface. Gently score the skull surface with sharp forceps to aid glue adherence. Apply a very thin layer of cyanoacrylate glue to the surface and allow the glue to dry thoroughly (**Fig. 4-2b**).
9. Attach a metal head fix bar to the skull, away from the area of the desired window with a small dab of cyanoacrylate glue and allow the glue to dry thoroughly (**Fig. 4-2k**). Then secure the connector with a layer of dental cement.

We adhere a custom-made bar, in this case with two attachment points (**Fig. 4-2j,k**). This greatly reduces the degrees of freedom and simplifies re-location of the same imaging field in longitudinal studies. A wide cross bar gives ample room for electrode placement and stimulation of vibrissae, if desired. The exact design of the head mount has varied considerably between labs and is often custom-designed to suit the needs of the experimenter. The head mount must be light-weight and relatively compact so that it does not impact the animal's movement and ability to obtain food and water within the cage. It is typically made from aluminum, stainless steel or titanium, precision-machined or laser cut to a fit atop the animals head. A secondary piece (also custom-designed) is necessary to affix the head to the restraint apparatus during imaging (**Fig. 4-2j**).

10. Cover the rest of the skull surface, excluding the location of the window, with a layer of dental cement (**Fig. 4-2c,d**). Ensure that all exposed edges of the skin are covered by cement.
11. Thin a 2 mm diameter region over the somatosensory cortex with a ½ mm burr. Alternate between wetting the skull with ACSF and then drying the skull surface with a

gentle stream of air from a pressurized dusting can; wet for cooling, and dry for thinning. The skull may bleed from the vessels in the inner cancellous layer, but can be controlled by flushing with ACSF (**Fig. 4-2e**). The skull begins to flex without breaking under the slight pressure of the drill when it is $\sim 50 \mu\text{m}$ thick, and the pial vessels should begin to be visible through the wet bone. Note that small white spots within the bone are visible immediately after the bone is moistened. The presence of these spots is used as a guide to estimate the thickness of the skull.

12. At this point, the bone must be thinned even further, and the speed and sharpness of the drill burr are critical. Change to a new drill burr and lightly shave the skull surface with small controlled movements while holding the drill like a pen. The shaving motions should move along the surface of the skull with the direction of bit rotation to minimize chatter; a drill speed of $\sim 10,000$ rpm is appropriate at this stage. The small white spots within the bone, normally visible when moistened bone is $\sim 50 \mu\text{m}$ thick, will not be visible at the final skull thickness of ~ 10 to $15 \mu\text{m}$ (**Fig. 4-2f**).
13. Polish the window region with tin oxide powder (**Fig. 4-2g**). Attach a pre-made drill bit that has been dipped in silicone aquarium sealant and withdrawn, leaving a tapered whip (**inset, Fig. 4-2g**). Place a small pinch of powder on the window along with a drop of ACSF. Agitate the slurry over the window for up to ten minutes by gently touching the tip of the moving whip to the skull surface. Surface irregularities and adherent bone chips left by drilling in the previous steps should be removed after polishing. Flush away the tin oxide powder thoroughly from the window using ACSF and dry the bone thoroughly with a gentle stream of air. Note that remaining tin oxide particles can become luminescent and interfere while imaging with TPLSM.
14. Cut small square pieces of no. 0 cover glass, roughly 2 by 2 mm, by gently scoring separated horizontal and vertical lines in the cover glass with a scribe. Then place the cover glass in a petri dish and shake vigorously to separate the glass pieces.
15. Apply a small dab of cyanoacrylate glue over the dry window using the wooden tip of a broken cotton-tipped applicator; stirring the glue helps to prevent the formation of bubbles. Next, quickly place an appropriately sized piece of no. 0 cover glass atop the glue (**Fig. 4-2h**). Using forceps, gently push the glass downward so that it is in contact with the skull surface. Quickly wipe away any excess wet glue above the window with a

Kimwipe twisted to a fine point. Allow the glue to dry thoroughly for 10 minutes before proceeding. Excess cyanoacrylate glue can be removed from the upper surface of the cover glass with a scalpel after it is dried.

16. Seal the edges of the cover glass with dental cement and form a slightly raised well around the window to hold water for the immersion objective (**Fig. 4-2i**).

Metabond from Parkell bonds more strongly to the skull than other cements tested and has been effective without skull screws. However, if increased stability is necessary, two self-tapping #000 screws can be added to the contralateral hemisphere of the skull prior to application of the dental cement (**Fig. 4-2k**), as described in past methods [10]

17. For some experiments, it may be desirable to inject dyes or insert electrodes into the tissue volume beneath the PoRTS window. A small hole can be added adjacent to the window, through which pipettes or electrodes can be introduced using a stereotaxic arm or Sutter manipulator [23]. This hole can be resealed with bone wax after the experiment if the animal is to be imaged again in future sessions.

18. Provide buprenorphine at a concentration of 0.03 mg per kg subcutaneously for analgesia and allow the animal to recover on a heat pad until fully awake.

3.2. Preparation for imaging

1. One to two days following surgery, stabilize the animal in a restraint apparatus, using the frame as a head support (**Fig. 4-2j**). The apparatus typically consists of an optical breadboard with miniature optomechanical components commercially available from Newport or ThorLabs.
2. Habituation to head-fixation is important to reduced animal movement during imaging. A new animal can be gradually accustomed to head restraint over a period of 3 to 7 days, starting with 15 min sessions without imaging and working up to several hours [14]. Head-restrained mice tend to struggle less when their bodies are enclosed within a loose-fitting plastic or cardboard tube.
3. The first two-photon imaging session should be at least 3 days after the initiation of habituation when the animal has become more accustomed to the apparatus. For each imaging session, restraining the animal for two hours at a time is reasonable, but times can differ for each animal. Discomfort should be gauged by the extent of struggling and

vocalizations emitted, and the restraint time adjusted accordingly. For imaging sessions lasting hours, drinking water should be supplied with a pipette.

In our experience some animals, approximately 10%, never become habituated to head-fixation and cannot be used for awake imaging.

4. Before imaging, the mouse must be briefly anesthetized with isoflurane for an intravenous injection of fluorescent dextran dye. Inject 25 to 50 μL of 5 % (w/v) fluorescent-dextran dye dissolved in saline either through the tail vein or infraorbital vein to label the blood serum. Use an ultra-fine 0.3 mL insulin syringe with 29.5 gauge needle. The dye will remain in circulation for approximately three to four hours, and supplements can be given as necessary if the animal is re-anesthetized. Intravenous injections are painful and must be done under general anesthesia.
5. Physical movement of the animal can be a source of artifacts in the data. In practice, a properly habituated animal will provide movement-free data for several minutes at a time even during sensory stimulation. Typically, several trials are collected for each stimulus paradigm and trials with excessive movement will be discarded. As a quality control measure, data acquisition can be tested on capillaries, which are only 3 to 5 μm in diameter and thus most sensitive to motion. Similarly, a surface arteriole, which may move due to dilations/constriction, can be scanned simultaneously with a neighboring venule that should exhibit little or no change in lumen diameter. A movement in both vessels would indicate movement of the animal. Low-cost accelerometers can be used to monitor movement of the animal and be recorded along side the vasodynamic measurements to identify data sets with excessive movement [14].

3.3 Measurement of blood flow dynamics in single cortical vessels

When the vasculature is labeled with an intravenous bolus of fluorescent-conjugated dextran, red blood cells (RBCs) exclude the high molecular weight dextran dye and will appear as dark shadows moving against a bright fluorescent background. This differential staining is the basis for measuring RBC velocity using laser-scanning microscopy [9, 24]. Conventionally, single line scans are used to sample the RBC velocity and diameter of a vessel separately [4, 25]. However, blood flow is dynamic and could change within the time between each scan. In order to collect more samples simultaneously and with varying trajectories within the imaging plane, we use custom software to direct the imaging laser beam in a user-defined path (**Fig. 4-3a**)

[26, 27], following earlier work [28-30]. Linear segments of constant scan speed traverse along the length of the center of the vessel and across the width of the vessel to measure RBC speed and lumen diameter, respectively (**right panel in Fig. 4-3a**). These linear scan segments are connected by polynomial splines, where connecting portions of the scan are accelerated to allow for rapid data collection across multiple vessels (**right panel in Fig. 4-3a**) [27]. The resulting line scan is a space-time image, typically displayed with the individual scan lines stacked on top of each other (**Fig. 4-3b**).

Figure 4-3 goes about here.

3.3.1. Calculating red blood cell velocity. Portions of the scan path along the centerline of the vessel lumen reveal angled streaks within the cascade image (**right panel in Fig. 4-3b**). Moving RBCs in flowing vessels sampled at a sufficient rate will appear as diagonal streaks. A stationary or stalled flow will result in vertical streaks. In the limiting case of extremely fast flowing vessels, the streaks will become horizontal and velocity data cannot be extracted. The centerline velocity is proportional to the slope of the RBC streaks, measured from vertical. This slope can be efficiently determined with a Radon transform of windowed portions of the data [31], which is available in the MATLABTM Image Processing Toolbox (Mathworks) (**Fig. 4-4**). The direction of flow can be extracted from the sign of the slope and the direction of the line scan sweep.

Figure 4-4 goes about here.

A velocity time series is calculated by taking successive time windowed portions of the line scan (**Fig. 4-4a**). The size of the window must be sufficiently short to resolve the highest velocity modulation frequency, the heart rate, which is 8 to 10 Hz for awake mice [14]. In addition, the window size must be large enough to capture enough streak lines so that the Radon transform has sufficient data to calculate an accurate velocity value, but small enough to prevent smoothing out the higher frequencies of the velocity data (**Fig. 4-4b**). We find that a window size of 40 ms is a good compromise, which yields a Nyquist frequency of 12.5 Hz. We further use a window spacing of 10 ms.

Oscillating physiological rhythms within the RBC velocity are a first indicator of good data quality. In addition to heart rate, other physiological signals detected in the RBC velocity may include breathing at ~ 1 to 2 Hz, and vasomotion at ~ 0.1 to 1 Hz [32, 33]. Breathing rate, however, is not always detectable in the flow data collected from awake mice (**Fig. 4-5**) [14].

Measurement of RBC velocity is the limiting factor for the measurement of flow in larger arterioles on the cortical surface. In practice, conventional galvanometric mirrors are sufficiently fast to simultaneously capture RBC velocity and diameter from one to two penetrating arteriole at a time in the anesthetized state. However, in the awake state RBC velocity tends to increase, and thus atypical fast scanning and/or special analysis techniques [34] may be necessary or smaller vessels should be sampled. Venules and deep microvessels exhibit slower RBC velocity and thus 3 to 4 vessels can be measured simultaneously with user defined line scans. Greater distances traversed by the laser will reduce the sampling frequency and a 1 to 2 kHz line scan rate is typically required for accurate sampling of the movement of RBCs in pial arterioles [27].

3.3.2. Calculating lumen diameter. As with the velocity calculation, the diameter calculation is taken from a time windowed portion of the data. The same window size and spacing used for velocity is typically used for diameter so that both parameters can be calculated on the same time scale. Vessel diameter is calculated as full-width at half-max of the vessel profile for each window (**left panel in Fig. 4-3b**). Note the intensity profile tends to increase near the edges due to the repulsion of RBCs from the glycocalyx, which generates two peaks. The two outermost half-max points of these peaks are used to calculate the vessel boundary. Linear interpolation is used to add subpixel accuracy to the diameter measurement.

3.3.3. Estimating the flux of red blood cells. There are two limiting cases for the flux. When the diameter of the vessel allows the passage of RBCs only in single file, as for the case of capillaries, the flux of RBCs is just the number of RBCs that pass per second [9, 35]. In this limit, the blood plasma has an essentially constant velocity profile as a function of distance from the center of the vessel, then the velocity falls rapidly to zero near the walls. The thin layer of plasma near the walls acts as a lubricating layer that, together with the glycocalyx, minimizes friction [36].

When the diameter of the vessel is much greater than that of the RBC, the flow is laminar and nearly parabolic as RBCs flow in parallel streams [4, 37]. The two vascular parameters, RBC velocity and lumen diameter, are combined to calculate the volume flux, *i.e.*, RBCs and plasma, for each vessel. Flux is a more complete description of blood flow in single vessels, as RBC speed and lumen diameter can change independently of each other [25, 38]. The volume flux through the vessel is given by

$$\bar{F} = \langle \bar{v} \rangle A = \frac{\pi}{8} \bar{v}(0) d^2$$

where $\langle \bar{v} \rangle$ is the average RBC velocity over A , the cross-sectional area of the vessel lumen, $\bar{v}(0)$ is the time-averaged RBC velocity at the center line of the vessel, and d is the lumen diameter. Note that this formula underestimates the flux as the nonzero spatial extent of the RBC flattens the parabola of Poiseuille flow; empirical corrections have been discussed [39] and a first-order correction was made.

4. Typical/anticipated results.

4.1. Stimulus induced changes in flux in the anesthetized rat. We measure the change in flux at the level of single pial vessels in response to somatosensory stimulation in rat anesthetized with alpha-chloralose (**Fig. 4-3c**). A line scan frequency of 733 Hz was used to capture the lumen diameter and RBC velocity of an arteriole and a venule nearly simultaneously. Both diameter and RBC velocity in the arteriole respond to stimulation (**left column in Fig. 4-3c**). The flux through the arteriole increases to a peak of 86 % over baseline, and contains contributions from both a change in diameter of 29 % and a change in velocity of 24 % taken (near) simultaneously from the same region of the vasculature. In contrast to the arteriole, a neighboring venule exhibits no change in lumen diameter, but a 23 % change in RBC velocity. Note that in both cases the increases in RBC velocity is partially masked by a peak in the underlying vasomotor fluctuation, but remains a significant increase over an average one-minute period of basal activity.

4.2. Vasodynamics in awake mice. Mice were habituated to head fixation (**Fig. 4-5a**) and blood flow was measured in single vessels through a chronically implanted PoRTS window (**Fig. 4-2**). The speed of RBCs within arterioles is high during the awake state and thus fast line-scanning frequencies, *i.e.*, 1 kHz or more, are required to capture this data. However, RBC velocity can be routinely measured within the full range of capillaries for awake mice [14, 20]. In this example, robust arteriole dilations could be evoked by prolonged contra-lateral whisker stimulation with puffs of air (**Fig. 4-5b**). Dilatory events consisted of an early peak followed by a secondary slowly-rising plateau, in averaged data, during sustained stimulation (**Fig. 4-5c**). The dilatory affect returned to baseline over ten seconds following cessation of

stimulation. Notably, spontaneous dilations observed during slow basal vasomotor activity were similar in magnitude to dilations evoked by stimulation, possibly indicating a common driving source (**Fig. 4-5d**). In both cases, the magnitude of dilation was larger with smaller diameter arterioles, *i.e.*, penetrating arterioles or vessels immediately feeding penetrating arterioles, rather than larger arterial branches. Pial venules, typically thought to be static in terms of diameter, show a weak dilation in the awake state (**Fig. 4-5c**). Overall, these data suggest that functional hyperemia changes detected by blood oxygen level dependent functional magnetic resonance imaging (BOLD fMRI) may be dominated by large changes in arteriole volume, in agreement with recent studies [40], rather than in venules as predicted by the “balloon” model [41].

Figure 4-5 goes about here.

Both basal and stimulated responses of arterioles and venules were strongly suppressed by the use of urethane, a common anesthetic [14], that can attenuate the magnitude of the overall dilatory response by up to 75 % in the anesthetized state. Other commonly used anesthetics, including isoflurane [42], α -chloralose [43], and propofol [44], similarly suppress the neurovascular response. In addition to the direct neural effects, anesthetics exert strong depressing effects on cardiovascular function [45]. Consistent with the depressive effects of anesthetics on neural and cardiovascular system, optical imaging studies of neurovascular coupling have found differences between the awake and anesthetized animal [46-48].

5. Future directions

The methodology described here fills an important gap in the existing range of tools for blood flow quantification and enables the study of vasodynamics in awake mice. While intrinsic optical imaging, laser speckle, and BOLD fMRI enable measurement of flow over broader areas of brain, two-photon microscopy complements these techniques and provides a view of dynamics at the resolution of individual small cortical vessels. Further, TPLSM can be concurrently used to examine activity of surrounding cells that could be driving vascular activity [49, 50]. This is important to dissect the basis of neurovascular coupling and bears direct relevance on clinical tools such as BOLD fMRI, as well as to examine vascular responses to disease states such as ischemic stroke.

It is becoming increasingly important to study cortical blood flow in the awake state, since anesthetics dampen the rich interplay between components of the neurovascular unit. To fully exploit vascular imaging in awake mice, some further advances will be necessary. First, faster laser-scanning is necessary to capture RBC velocity within larger cortical arterioles. Acousto-optic modulators [51] can in principle scan vessels with faster flow as well as sample from larger populations of vessels simultaneously. Recent advances in processing of line-scan data using particle image velocimetry will also be useful to assess RBC velocity in larger vessels [40]. Second, physiological parameters most relevant to blood flow including blood pressure and blood gas remain difficult to measure in awake mice. In particular, even when these parameters are measured invasively from catheters in peripheral vessels, they may not reflect what is happening in the cerebral vessel being examined. Novel imaging probes need to be developed to assess real-time changes in blood pressure, gas and pH at the vessel being examined. Finally, new tools to manipulate cell-specific vasoactive signaling cascades will be an important step in dissecting the chemical basis of neurovascular coupling [52].

Acknowledgements

We thank the National Institutes of Health for generous support through grants NS085402 to AYS, NS078168 and NS079737 to PJD and EB003832, MH085499, MH072570, and OD006831 to DK. AYS is also supported by The Dana Foundation and the South Carolina Clinical and Translational Institute, through NIH Grant number UL1 TR000062.

Literature cited.

1. Magistretti, P.J. and L. Pellerin, *Cellular mechanisms of brain energy metabolism and their relevance to functional brain imaging*. Philosophical Transactions of the Royal Society of London, 1999. **354**: p. 1155-1163.
2. Attwell, D. and S.B. Laughlin, *An energy budget for signaling in the grey matter of the brain*. Journal of Cerebral Blood Flow & Metabolism, 2001. **21**: p. 1133-1145.
3. Mchedlishvili, G., *Arterial Behavior and Blood Circulation in the Brain* 1963, New York: Consultants Bureau.
4. Schaffer, C.B., B. Friedman, N. Nishimura, L.F. Schroeder, P.S. Tsai, F.F. Ebner, P.D. Lyden, and D. Kleinfeld, *Two-photon imaging of cortical surface microvessels reveals a robust redistribution in blood flow after vascular occlusion*. Public Library of Science Biology, 2006. **4**: p. 258-270.
5. Blinder, P., A.Y. Shih, C.A. Rafie, and D. Kleinfeld, *Topological basis for the robust distribution of blood to rodent neocortex*. Proceedings of the National Academy of Sciences USA, 2010. **107**: p. 12670-12675.
6. Devor, A., P. Tian, N. Nishimura, I.C. Teng, E.M. Hillman, S.N. Narayanan, I. Ulbert, D.A. Boas, D. Kleinfeld, and A.M. Dale, *Suppressed neuronal activity and concurrent arteriolar vasoconstriction may explain negative blood oxygenation level-dependent signaling*. Journal of Neuroscience, 2007. **27**: p. 4452-4459.
7. Derdikman, D., R. Hildesheim, E. Ahissar, A. Arieli, and A. Grinvald, *Imaging spatiotemporal dynamics of surround inhibition in the barrels somatosensory cortex*. Journal of Neuroscience, 2003. **23**: p. 3100-3105.
8. Blinder*, P., P.S. Tsai*, J.P. Kaufhold, P.M. Knutsen, H. Suhl, and D. Kleinfeld, *The murine cortical angiome: A fully interconnected network of microvasculature that supports restricted blood flow*. Nature Neuroscience, 2013: p. in press.
9. Kleinfeld, D., P.P. Mitra, F. Helmchen, and W. Denk, *Fluctuations and stimulus-induced changes in blood flow observed in individual capillaries in layers 2 through 4 of rat neocortex*. Proceedings of the National Academy of Sciences USA, 1998. **95**: p. 15741-15746.
10. Shih, A.Y., J.D. Driscoll, P.J. Drew, N. Nishimura, C.B. Schaffer, and D. Kleinfeld, *Two-photon microscopy as a tool to study blood flow and neurovascular coupling in the rodent brain*. Journal of Cerebral Blood Flow & Metabolism, 2012. **32**: p. 1277-1309.
11. Helmchen, F. and D. Kleinfeld, *In vivo measurements of blood flow and glial cell function with two-photon laser scanning microscopy*. Methods in Enzymology, 2008. **444**: p. 231-254.
12. Franks, N.P., *General anaesthesia: From molecular targets to neuronal pathways of sleep and arousal*. Nature Reviews Neuroscience, 2008. **9**: p. 370-386.
13. Thrane, A.S., V. Rangroo-Thrane, D. Zeppenfeld, N. Loua, Q. Xua, E.A. Nagelhus, and M. Nedergaard, *General anesthesia selectively disrupts astrocyte calcium signaling in the awake mouse cortex*. Proceedings of the National Academy of Sciences USA, 2012. **109**: p. 18974-18979.
14. Drew, P.J., A.Y. Shih, and D. Kleinfeld, *Fluctuating and sensory-induced vasodynamics in rodent cortex extends arteriole capacity*. Proceedings of the National Academy of Sciences USA, 2011. **108**: p. 8473-8478.

15. Holtmaat, A., T. Bonhoeffer, D.K. Chow, J. Chuckowree, V. De Paola, S.B. Hofer, M. Hübener, T. Keck, G. Knott, W.C. Lee, R. Mostany, T.D. Mrsic-Flogel, E. Nedivi, C. Portera-Cailliau, K. Svoboda, J.T. Trachtenberg, and L. Wilbrecht, *Long-term, high-resolution imaging in the mouse neocortex through a chronic cranial window*. Nature Protocols, 2009. **4**: p. 1128-1144.
16. Mostany, R. and C. Portera-Cailliau, *A method for 2-photon imaging of blood flow in the neocortex through a cranial window*. Journal of Visualized Experiments, 2008. **12**: p. <http://www.jove.com/video/678>.
17. Yang, G., F. Pan, C.N. Parkhurst, J. Grutzendler, and W.B. Gan, *Thinned-skull cranial window technique for long-term imaging of the cortex in live mice*. Nature Protocols, 2010. **5**: p. 201-208.
18. Xu, H.T., F. Pan, G. Yang, and W.B. Gan, *Choice of cranial window type for in vivo imaging affects dendritic spine turnover in the cortex*. Nature Neuroscience, 2007. **10**: p. 549-551.
19. Kobat, D., M.E. Durst, N. Nishimura, A.W. Wong, C.B. Schaffer, and C. Xu, *Deep tissue multiphoton microscopy using longer wavelength excitation*. Optics Express, 2009. **17**: p. 13354-13364.
20. Drew, P.J., A.Y. Shih, J.D. Driscoll, P.M. Knutsen, D. Davalos, P. Blinder, K. Akassoglou, P.S. Tsai, and D. Kleinfeld, *Chronic optical access through a polished and reinforced thinned skull*. Nature Methods, 2010. **7**: p. 981-984.
21. Shih, A.Y., P.J. Drew, C. Mateo, P.S. Tsai, and D. Kleinfeld, *A polished and reinforced thinned skull window for long-term imaging and optical manipulation of the mouse cortex*. Journal of Visualized Experiments, 2012: p. <http://www.jove.com/video/3742>.
22. Cetin, A., S. Komai, M. Eliava, P.H. Seeburg, and P. Osten, *Stereotaxic gene delivery in the rodent brain*. Nature Protocols, 2006. **1**: p. 3166-3173.
23. Stosiek, C., O. Garaschuk, K. Holthoff, and A. Konnerth, *In vivo two-photon calcium imaging of neuronal networks*. Proceedings of the National Academy of Sciences USA, 2003. **100**: p. 7319-7324.
24. Villringer, A., R.L. Haberl, U. Dirnagl, F. Anneser, M. Verst, and K.M. Einhaupl, *Confocal laser microscopy to study microcirculation on the rat brain surface in vivo*. Brain Research, 1989. **504**: p. 159-160.
25. Shih, A.Y., B. Friedman, P.J. Drew, P.S. Tsai, P.D. Lyden, and D. Kleinfeld, *Active dilation of penetrating arterioles restores red blood cell flux to penumbral neocortex after focal stroke*. Journal of Cerebral Blood Flow & Metabolism, 2009. **29**: p. 738-751.
26. Valmianski, I., A.Y. Shih, J. Driscoll, D.M. Matthews, Y. Freund, and D. Kleinfeld, *Automatic identification of fluorescently labeled brain cells for rapid functional imaging*. Journal of Neurophysiology, 2010. **104**: p. 1803-1811.
27. Driscoll, J.D., A.Y. Shih, P.J. Drew, G. Cauwenberghs, and D. Kleinfeld, *Two-photon imaging of blood flow in cortex*, in *Imaging in Neuroscience: A Laboratory Manual*, F. Helmchen, A. Konnerth, and R. Yuste, Editors. 2011, Cold Spring Harbor Laboratory Press: New York. p. 927-938.
28. Göbel, W., B.M. Kampa, and F. Helmchen, *Imaging cellular network dynamics in three dimensions using fast 3D laser scanning*. Nature Methods, 2007. **4**: p. 73-79.
29. Göbel, W. and F. Helmchen, *New angles on neuronal dendrites in vivo*. Journal of Neurophysiology, 2007. **98**: p. 3770-3779.

30. Lillis, K.P., A. Eng, J.A. White, and J. Mertz, *Two-photon imaging of spatially extended neuronal network dynamics with high temporal resolution*. Journal of Neuroscience Methods, 2008. **172**: p. 178-184.
31. Drew, P.J., P. Blinder, G. Cauwenberghs, A.Y. Shih, and D. Kleinfeld, *Rapid determination of particle velocity from space-time images using the Radon transform*. Journal of Computational Neuroscience, 2010. **29**: p. 5-11.
32. Kleinfeld, D. and P.P. Mitra, *Applications of spectral methods in functional brain imaging*, in *Imaging: A Laboratory Manual*, R. Yuste, Editor 2011, Cold Spring Harbor Laboratory Press, New York. p. 12.1-12.7.
33. Mayhew, J.E.W., S. Askew, Y. Zeng, J. Porrill, G.W.M. Westby, P. Redgrave, D.M. Rector, and R.M. Harper, *Cerebral vasomotion: 0.1 Hz oscillation in reflectance imaging of neural activity*. Neuroimage, 1996. **4**: p. 183-193.
34. Kim, T.N., P.W. Goodwill, Y. Chen, S.M. Conolly, C.B. Schaffer, D. Liepmann, and R.A. Wang *Line-scanning particle image velocimetry: An optical approach for quantifying a wide range of blood flow speeds in live animals*. Public Library of Science ONE, 2012. **P7**: p. e38590.
35. Chuquet, J., L. Hollender, and E.A. Nimchinsky, *High-resolution in vivo imaging of the neurovascular unit during spreading depression*. Journal of Neuroscience, 2007. **27**: p. 4036-4044.
36. Secomb, T.W., R. Hsu, and A.R. Pries, *A model for red blood cell motion in glycocalyx-lined capillaries*. American Journal of Physiology - Heart and Circulatory Physiology, 1998. **274**: p. H1016-H1022.
37. Rovainen, C.M., T.A. Woolsey, N.C. Blocher, D.-B. Wang, and O.F. Robinson, *Blood flow in single surface arterioles and venules on the mouse somatosensory cortex measured with videomicroscopy, fluorescent dextrans, nonoccluding fluorescent beads, and computer-assisted image analysis*. Journal of Cerebral Blood Flow & Metabolism, 1993. **13**: p. 359-371.
38. Kontos, H.A., *Validity of cerebral arterial blood flow calculations from velocity measurements*. Stroke, 1989. **20**: p. 1-3.
39. Nishimura, N., N.L. Rosidi, C. Iadecola, and C.B. Schaffer, *Limitations of collateral flow after occlusion of a single cortical penetrating arteriole*. Journal of Cerebral Blood Flow & Metabolism, 2010. **30**: p. 1914-1927.
40. Kim, T. and S.G. Kim, *Temporal dynamics and spatial specificity of arterial and venous blood volume changes during visual stimulation: Implication for BOLD quantification*. Journal of Cerebral Blood Flow & Metabolism, 2011. **31**: p. 1211-1222.
41. Buxton, R.B., E.C. Wong, and L.R. Frank, *Dynamics of blood flow and oxygenation changes during brain activation: The balloon model*. Magnetic Resonance in Medicine, 1998. **39**: p. 855-864.
42. Takuwaa, H., T. Matsuura, T. Obataa, H. Kawaguchia, I. Kannoa, and H. Ito, *Hemodynamic changes during somatosensory stimulation in awake and isoflurane-anesthetized mice measured by laser-Doppler flowmetry*. Brain Research, 2012. **1472**: p. 107-112.
43. Dudley, R.E., S.R. Nelson, and F. Samson, *Influence of chloralose on brain regional glucose utilization*. Brain Research, 1982. **233**: p. 173-180.

44. Alkire, M.T., R.J. Haier, S.J. Barker, N.K. Shah, J.C. Wu, and Y.J. Kao, *Cerebral metabolism during propofol anesthesia in humans studied with positron emission tomography*. *Anesthesiology*, 1995. **82**: p. 393-403.
45. Janssen, B.J., T. De Celle, J.J. Debets, A.E. Brouns, M.F. Callahan, and T.L. Smith, *Effects of anesthetics on systemic hemodynamics in mice*. *American Journal of Physiology: Heart and Circulatory Physiology*, 2004. **287**: p. H1618–H1624.
46. Nakao, Y., Y. Itoh, T.Y. Kuang, M. Cook, J. Jehle, and L. Sokoloff, *Effects of anesthesia on functional activation of cerebral blood flow and metabolism*. *Proceedings National Academy of Sciences USA*, 2001. **98**: p. 7593–7598.
47. Jones, M., I.M. Devonshire, J. Berwick, C. Martin, P. Redgrave, and J. Mayhew, *Altered neurovascular coupling during information-processing states*. *European Journal of Neuroscience*, 2008. **27**: p. 2758-2772.
48. Martin, C., M. Jones, and J. Martindale, *Haemodynamic and neural responses to hypercapnia in the awake rat*. *European Journal of Neuroscience*, 2006. **24**: p. 2601-2610.
49. Takano, T., G.F. Tian, W. Peng, N. Lou, W. Libionka, X. Han, and M. Nedergaard, *Astrocyte-mediated control of cerebral blood flow*. *Nature Neuroscience*, 2006. **9**: p. 260-267.
50. Nizar, K., H. Uhlirva, P. Tian, P.A. Saisan, Q. Cheng, L. Reznichenko, K.L. Weldy, T.C. Steed, S.V. B., C.L. Macdonald, J. Cui, S.L. Gratiy, S. Sakadzic, D.A. Boas, T.I. Beka, G.T. Einevoll, J. Chen, E. Masliah, A.M. Dale, G.A. Silva, and A. Devor, *Stimulus-induced vasodilation occurs without IP3 receptor activation and may precede astrocytic calcium increase*. *Journal of Neuroscience*, 2013. **33**: p. 8411-8422.
51. Lechleiter, J.D., D.T. Lin, and I. Sieneart, *Multi-photon laser scanning microscopy using an acoustic optical deflector*. *Biophysical Journal*, 2002. **83**: p. 2292-2299.
52. Kleinfeld, D., P. Blinder, P.J. Drew, J.D. Driscoll, A. Muller, P.S. Tsai, and A.Y. Shih, *A guide to delineate the logic of neurovascular signaling in the brain*. *Frontiers in Neuroenergetics*, 2011. **1**: p. 1-9.

Figure captions

Figure 4-1. The vasculature of the mouse cortex. (a) Example of vectorized data obtained throughout the full depth of cortex and extending into the white matter. Surface and penetrating arterioles are colored red, venules blue, and the borders of cortical columns denoted by a golden band. **(b)** A s selected slice from the larger data set in panel a that illustrates the extent of penetrating vessels. Adapted from Blinder, Tsai, *et al.* [8]. Reproduced by permission of Nature publishing group © 2013.

Figure 4-2. Realization and benefits of a PoRTS transcranial window in mouse. (a to i) Images of the different stages in the procedure for generating a chronic PoRTS window. β = bregma and λ = lambda. **(j)** Custom-machined cross bar head mount for awake preparations. The cross bar greatly reduces degrees of freedom for repeated imaging of the same location within the window. In this example, a connector was also implanted for repeated electrocorticogram recordings. **(k)** Schematic diagram showing dorsal view of the head mount and position of various components. Two #000 self-tapping screws can be added with the cross bar mount for added stability when imaging awake preparations. **(l)** Schematic diagram showing cross section of a PoRTS window. **(m)** Maximum z-axis projections across 65 μm of fluorescein-conjugated-dextran filled vasculature through a PoRTS window 90 days after surgery. Each image is the average of six frames, the z-step was 2 μm , the dwell time was 3 μs per pixel and the average power was 25 to 120 mW. **(n)** Subsurface microvessels are stable under the PoRTS window for over a month after implantation. Images show maximum projections across 20 to 70 μm below the surface using an average of 5 frames, a dwell time of 6 μs per pixel, and an average power of 30 to 45 mW. Panels a to l adapted from Shih *et al.* [10]; panels m and n adapted from Drew *et al.* [20]. Reproduced by permission of Nature publishing group © 2012.

Figure 4-3. Simultaneous measurement of diameter and velocity in two vessels in somatosensory cortex of a Sprague Dawley rat using a spatially optimized line scan. The animal is anesthetized with alpha-chloralose. **(a)** Image of fluorescently stained vessels. The forelimb and hindlimb representations across cortex were mapped using intrinsic optical imaging. The expanded view shows the scan path, with the colored segments corresponding

to scan regions when the mirrors moved at constant velocity and interconnecting white lines as regions when the mirrors were accelerated to reduce total scan time. **(b)** The scanning procedure. The top trace is the mirror speed as a function of time. Portions used to acquire diameter and velocity data are constant speed. The line-scans generated from the path are stacked sequentially as a function of time to produce a raw cascade image. The diameter is calculated as the full-width half-maximum of a time-average of several scans across the width of a vessel. Red blood cell velocity is calculated from the angle of the RBC streaks. **(c)** Data traces of diameter, velocity, and flux for the arteriole and venule, before, during, and after simulation of the forelimb, processed to remove heart rate and smoothed with a running window. Both vessels show an increase in flux in response to stimulation. Adapted from Driscoll *et al.* [27]. Reproduced by permission of Cold Spring Harbor Laboratory Press © 2011.

Figure 4-4. Illustration of the Radon method to determine RBC velocity. **(a)** Raw line-scan image data from a subsurface vessel. White, vertical lines show the spatial range selected for analysis. The yellow lines show the temporal windowing. The data blocks to the right are overlapping windows of data that are ready for processing, denoted $F_i(x, t)$ where i is an index in units of $T/4$, where $T = 25$ ms is the duration of the data block and $L = 300$ μm is the length of the useable line-scan. **(b)** The top image shows the Radon transform of the first data block. The plot below shows the normalized variance of the Radon transform. The peak is at $\theta_{\text{max}} = 65^\circ$, which corresponds to a RBC velocity of $v(0) \equiv (\Delta x / \Delta t) \cdot \cot(\theta_{\text{max}})$, where $\Delta x = 1.0$ μm is the pixel width and $\Delta t = 0.5$ ms is time per line, so that $v(0) = 0.93$ mm/s is calculated. Adapted from Drew *et al.* [31]. Reproduced by permission of Springer Science + Business Media © 2010.

Figure 4-5. Spontaneous and stimulus-induced vascular dynamics in the cortex of awake mouse. **(a)** Schematic of the experimental setup. The awake mouse is head-fixed by means of a bolt and sits passively in an acrylic cylinder beneath the two-photon microscope. An air puffer for sensory stimulation is aimed at the vibrissae. The insert shows an image of surface vessels. **(b)** Single trial time-series of the diameter of an arteriole in response to a 30 s period of stimulation. Note the spontaneous dilations. **(c)** Plot of peak averaged dilation responses to 30 s vibrissae stimulation. Early arterial peaks, in the 0 to 10 s interval after

stimulation, are denoted by red circles; regression slope = $0.007 \mu\text{m}^{-1}$ ($r^2 = 0.15$, $p < 0.02$). Late arterial peaks, greater than 10 s after onset, are denoted by red triangles; the linear regression is not significant. Venules are denoted by blue dots; the linear regression is not significant. **(d)** Plot of peak spontaneous dilations for arteries, in red, and veins, in blue. Grey area shows the $0.2 \mu\text{m}$ resolution limit of detectable changes. Lines show linear regressions; slope of $-0.004 \mu\text{m}^{-1}$ for arterioles is significant ($r^2 = 0.13$, $p < 0.001$), while that for veins is not significantly different from zero. Adapted from Drew *et al.* [14]. Reproduced by permission of the National Academy of sciences © 2011.

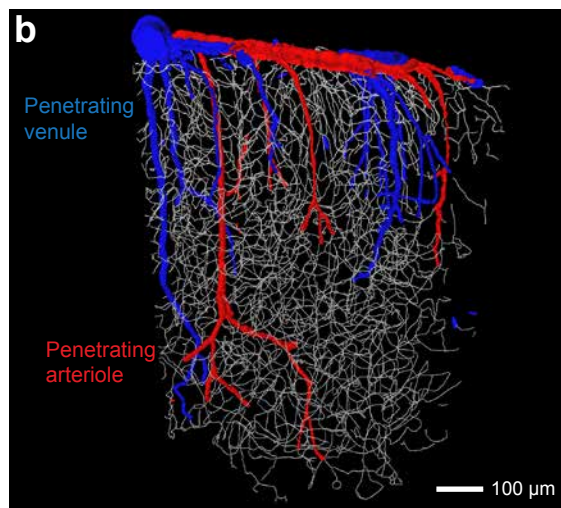
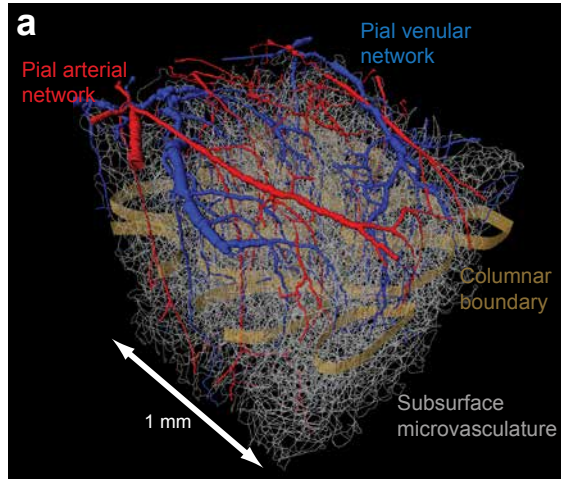


Figure 1 - Shih, Drew and Kleinfeld

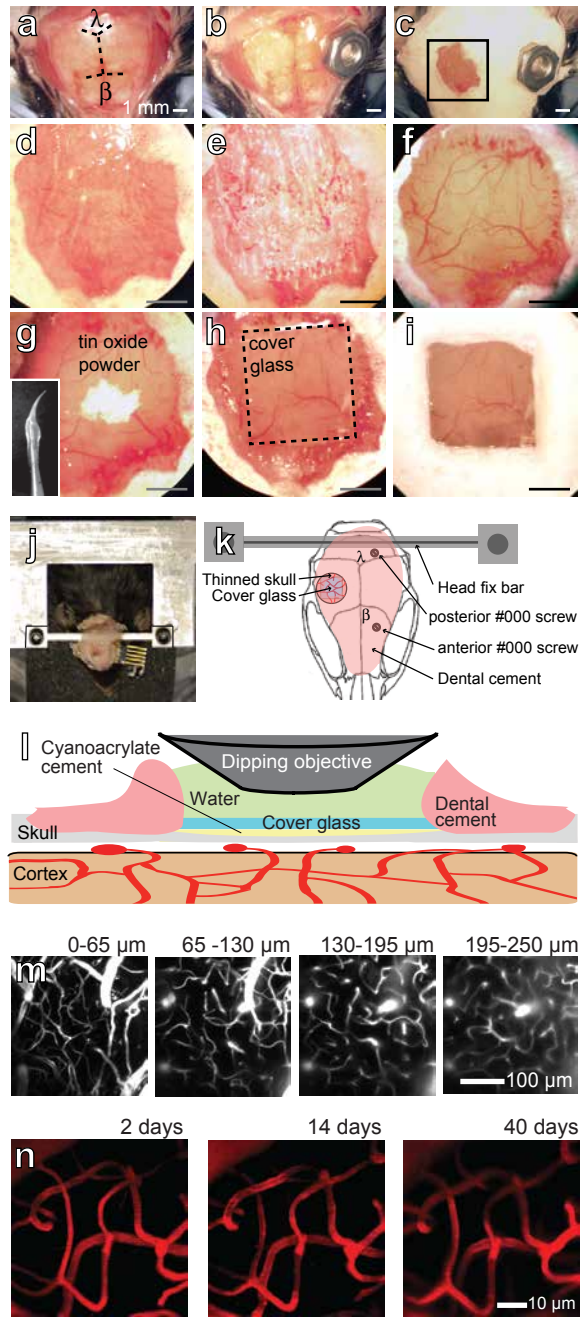


Figure 2 - Shih, Drew and Kleinfeld

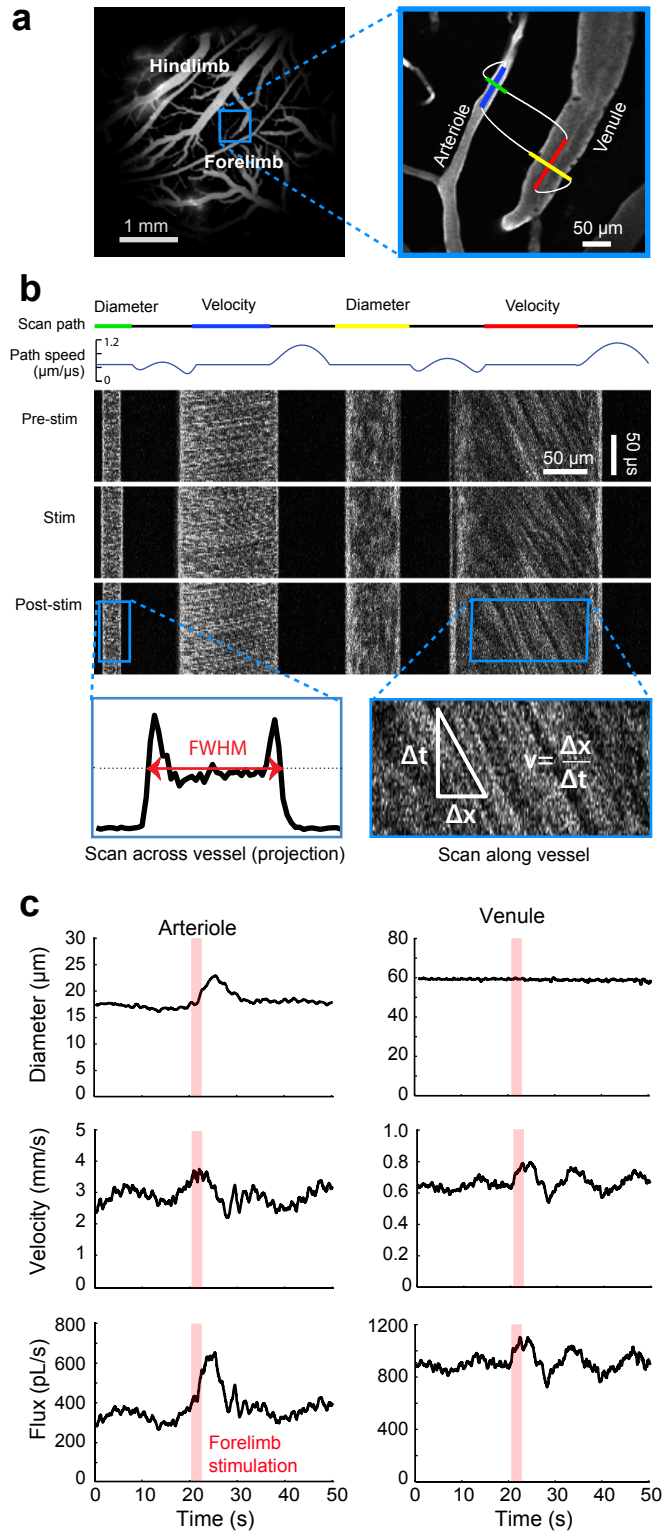


Figure 3 - Shih, Drew and Kleinfeld

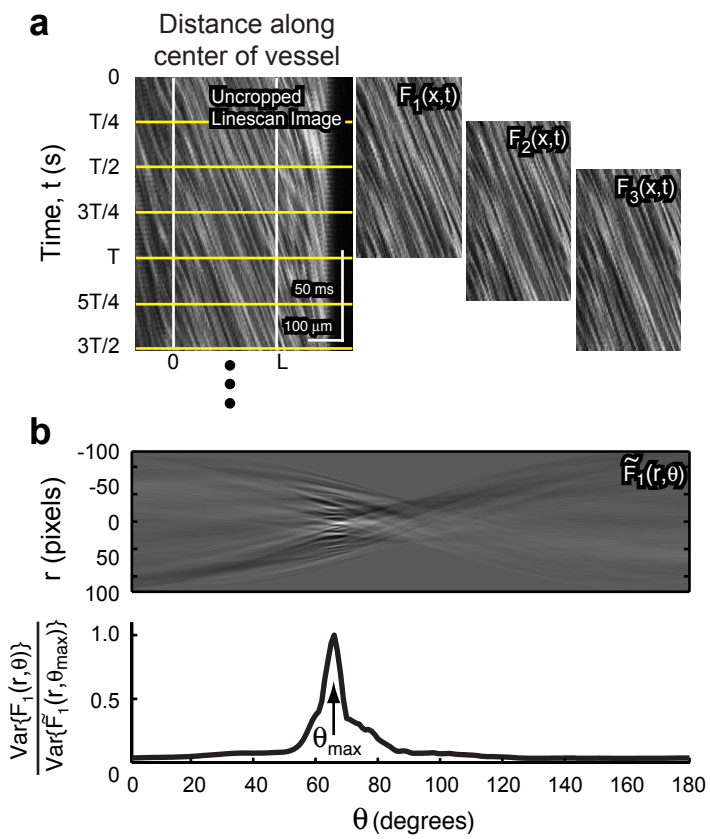


Figure 4 - Shih, Drew and Kleinfeld

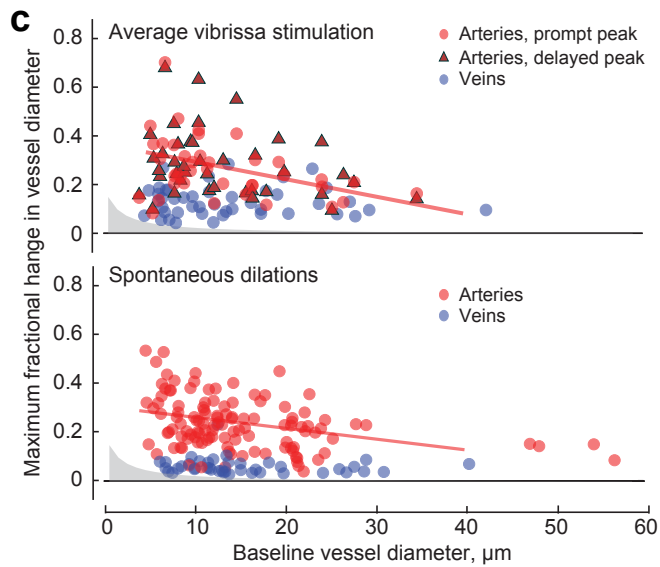
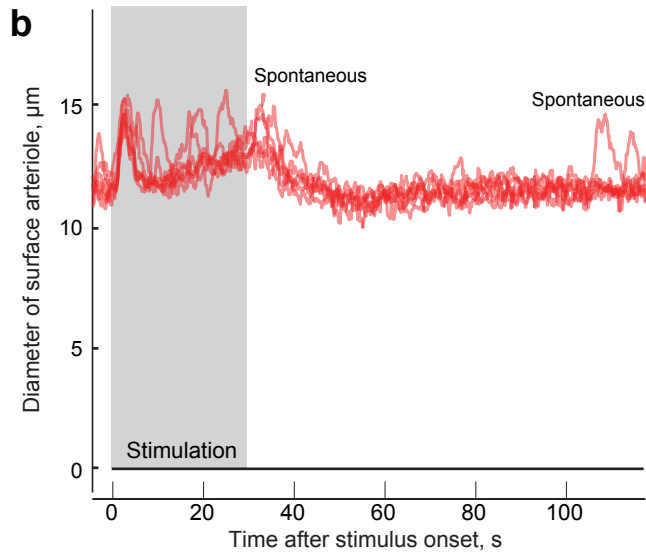
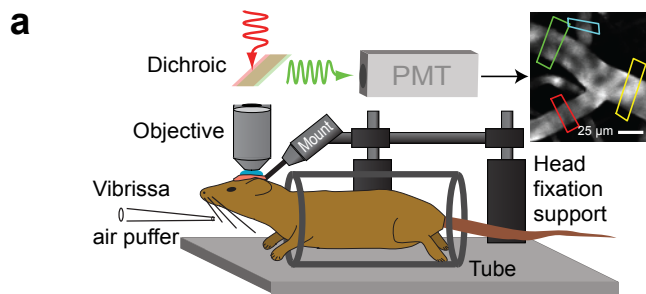


Figure 5 - Shih, Drew and Kleinfeld